Alcohol induced ultra-fine dispersion of Pt on tuned morphologies of CeO_2 for CO oxidation

Sumanta Kumar Meher [a], Matteo Cargnello [b], Horacio Troiani [c], T. Montini [b], G. Ranga Rao [a],*, Paolo Fornasiero [b],**

[a] Department of Chemistry, Indian Institute of Technology Madras, Chennai 600036, India
[b] Department of Chemical and Pharmaceutical Sciences, INSTM Trieste Unit, ICCOM-CNR Trieste Research Unit and Center of Excellence for Nanostructured Materials (CENMAT), University of Trieste, via L. Giorgieri 1, 34127 Trieste, Italy
[c] Centro Atómico Bariloche (CNEA) and Instituto Balseiro (UNCuyo), Consejo Nacional de Investigaciones Científicas y Técnicas (CONICET), (8400) S.C. de Bariloche, A. Bustillo km 9.5, Río Negro, Argentina

ARTICLE INFO

ABSTRACT

Controlling the structures of supports and supported phases is important for catalytic applications where synergic effects can play a main role. In this context, we present versatile methods for suitable microstructurization of CeO_2 support and improved dispersion of supported Pt crystallites in a Pt/CeO_2 system for enhanced catalytic oxidation of CO. The physicochemical properties investigated using SEM, BET, visible Raman, H_2-TPR and OSC measurements demonstrated the important role played by the precursor on the properties of CeO_2. Further, 0.5 wt% Pt deposited over CeO_2 via ethylene glycol assisted reduction (EGR) was found to be more advantageous than conventional impregnation (IMP) in producing very finely dispersed Pt particles that did not noticeably sinter even after thermal treatment at 500 °C for longer duration. H_2-chemisorption and H_2-TPR experiments further substantiated better Pt dispersion on CeO_2 prepared in the presence of Cl^- ions regardless of the method employed, thus suggesting a strong microstructural effect of support during growth and anti-sintering activity of Pt crystallites. The CO oxidation activity additionally demonstrates that samples prepared by EGR method show remarkably better performance (100% conversion in <100 °C) as compared to their impregnated counterparts (100% conversion at ~300 °C). The present approach to improve the catalytic activity of Pt/CeO_2 based hetero-nanocomposites by finely dispersing low concentrations of Pt nanocrystallites over microstructurally tuned CeO_2 support is encouraging in the context of designing novel metal–metal oxide based catalysts for astute potential applicability under vibrantly testing conditions.

© 2012 Elsevier B.V. All rights reserved.

1. Introduction

Supported metal catalysts with high activity and selectivity are of utmost importance since decades for pollution control and in general environmental applications [1]. Among such catalytic processes, oxidation of CO $(CO + O_2 \rightarrow CO_2)$ is of paramount importance given the environmentally hazardous nature of this molecule. However, the typically forbidden energetic, geometric and electronic (spin forbidden, since total spin of reactants and products are 1 and 0, respectively) issues make the gas phase oxidation of CO rather difficult [2,3]. Hence the most rational approach to oxidize CO has been the use of a catalyst with suitable active sites capable of adsorbing and combining CO and O_2 molecules to produce

CO_2 [2,3]. To this aim, noble metals in the form of nanocrystals which are highly prone to chemisorption of CO (via metal–C bond and not metal–O bond), and metal oxides with appreciable oxygen vacancy (high oxygen storage capacity) which are best favorable sites for O_2 adsorption provide ideally synergistic condition for CO oxidation, although the atomic level interactions during the whole process is exceedingly complex [4–6]. Many metal–metal oxide combinations have been investigated so far which show substantial activity for catalytic oxidation of CO by O_2 even at sub-ambient temperature [7–13]. Among these vast possibilities, the Pt/CeO_2 system has been one of the most studied and found to be highly active and stable [14–19]. Here, the strong $Pt–CeO_2$ interaction (a complex charge transfer phenomena) promotes the anti-sintering of Pt crystallites on CeO_2 surface during reactions at elevated temperature [3,20,21]. In addition, CeO_2 is known as an excellent redox support due to its superior physicochemical properties, and large number of oxygen vacancies owing to facile Ce^{4+}/Ce^{3+} redox transition, with significant oxygen mobility and oxygen storage capacity (OSC) even at elevated temperature [22].

These remarkable physicochemical and electronic properties make Pt/CeO$_2$ very promising for facile oxidation of CO under cycling conditions.

Structural modification of metals and metal oxides in nano- as well as micro- scale dimension greatly allows the possible manipulation of crystallographic orientations, which essentially influence the surface atom densities, electronic structure and chemical reactivity [23]. For this reason, the deliberate design of particular surface morphology/microstructure can lead to enhanced reducibility, oxygen vacancy, OSC and reactivity of CeO$_2$ [24]. Structurally designed CeO$_2$ with specifically oriented crystals, small crystallite size and large number of accessible surface active sites can outperform conventional materials. For example, it has been shown that nanowire and nanorods of CeO$_2$ predominantly exposing (1 0 0) and (1 1 0) faces are more active for CO oxidation than nanoparticles of CeO$_2$ with exposed (1 1 1) surface [25]. Some of us recently reported that nanorods of CeO$_2$ exposing (1 0 0) and (1 1 0) crystalline facets possess high reducibility, oxygen vacancy and oxygen storage capacity, which are by far more active for soot oxidation reaction [26]. In addition to the structure of the support, nanocrystallites of Pt with tuned size, shape, and crystallographic orientation show characteristic reactivity, activity and selectivity for appropriate applications [27]. In this context, it is well known that the dissociation of CO as well as O$_2$ occurs preferentially at step sites of Pt, and the CO adsorbed at Pt(1 1 1) terraces is more active compared with CO at Pt(1 0 0) step sites, while adsorbed O$_2$ at step sites is more active [28]. Further, the small crystallite size and finer dispersions of Pt on the support provide superior metal–support interface which is essentially the most active site for CO oxidation [29]. Utilization of Pt is essential to provide suitable active sites and lower the activation energy for facile oxidation of CO on a redox support, but its high cost brings limitation for extensive commercial exploitation. The utilization of very small concentrations of Pt and its concomitant optimal dispersion on the support surface are crucial in the context of catalyst development for commercial exploitation. A further concern is related to the typically high tendency to segregation and sintering of ultrafine Pt crystallites dispersed on CeO$_2$ support under high reaction temperatures which consequences in the drastic decrease of catalytic activity [17–29]. Hence suitable microstructure of CeO$_2$ which can limit the sintering of dispersed Pt crystallites is essential for utilization under testing thermal conditions. Although several attempts have been made in the literature to individually address these problems in separate Pt/CeO$_2$ systems, there is a lack of collective formulation to deal with all these issues in a single Pt/CeO$_2$ system.

In this report we have specifically prepared tuned surface morphologies of CeO$_2$ by controlled precipitation and using precursors with different counter anions in the reaction medium. Structure–property correlations of different CeO$_2$ samples have been established from detailed physicochemical studies. In addition, a versatile method has been adopted for ultra-fine dispersion of very low amount (0.5 wt%) of Pt on the CeO$_2$ support to prepare Pt/CeO$_2$ based heteronanocomposites. Further, the influence of support microstructure on the dispersion and stability (at high temperature) of Pt has been studied. It was found that a suitable combination of support microstructure and Pt dispersion can be ideal to achieve high efficiency for CO oxidation.

2. Experimental

2.1. Materials

Analytical grade cerium nitrate hexahydrate (Ce(NO$_3$)$_3$·6H$_2$O (99.9%, SD Fine, India)), cerium chloride hexahydrate (CeCl$_3$·6H$_2$O (99.9%, Sigma–Aldrich)), cetyltrimethylammonium bromide (CTAB, (C$_{16}$H$_{33}$)N(CH$_3$)$_3$Br, (99.9%, Sigma–Aldrich), urea ((CO(NH$_2$)$_2$, 99%, Thomas-Baker) and chloroplatinic acid hexahydrate (H$_2$PtCl$_6$·6H$_2$O, Sigma–Aldrich) with ≥37.50% Pt basis were used as received. Laboratory prepared triple distilled water was used during all the experimental processes.

2.2. Preparation of nanostructured CeO$_2$

In a typical synthesis, 20 mM of cerium salt was dissolved in 100 mL of water, which was then added dropwise to 100 mL of 10 mM aqueous CTAB solution. After 1 h stirring, 80 mM of solid urea was added and the solution was further stirred for 3 h to make it homogeneous. The whole solution was then transferred into a Teflon lined stainless steel autoclave (250 mL capacity) and was heated to 120 °C for 24 h in an electric oven. The autoclave was then self-cooled to room temperature, and a white color precipitate (precursor) was isolated by centrifugation followed by repeated washing with water, mixture of ethanol and water, and pure ethanol. The precipitate was then dried under vacuum at 60 °C for overnight. The materials prepared using Ce(NO$_3$)$_3$·6H$_2$O and CeCl$_3$·6H$_2$O are designated as COCH−NH and COCH−CH, respectively. After calcination of COCH−NH and COCH−CH at 500 °C (with a heating ramp of 5 °C min^{-1}) for 3 h in flowing air, the CeO$_2$ products were obtained, which were designated as CeO$_2$−NH and CeO$_2$−CH, respectively.

2.3. Preparation of 0.5 wt% Pt loaded CeO$_2$ by conventional impregnation (IMP) method

In this process, 500 mg of either CeO$_2$−NH or CeO$_2$−CH sample was thoroughly dispersed in water by constantly stirring for 12 h. Appropriate amount of aqueous H$_2$PtCl$_6$·6H$_2$O solution was then added drop-wise to the above mixture and further stirred for 12 h. The resultant mixture was then slowly heated under constant stirring until complete evaporation of water and the solid product was further dried under vacuum at 60 °C for overnight. Subsequently, the dried sample was calcined at 500 °C (with a heating ramp of 5 °C min^{-1}) for 3 h in flowing air to obtain the Pt loaded CeO$_2$ samples. The loading of Pt on the CeO$_2$ samples was fixed at 0.5 wt%, and the final samples prepared by using CeO$_2$−NH and CeO$_2$−CH as supports were designated as Pt/CeO$_2$−NH_IMP and Pt/CeO$_2$−CH_IMP, respectively.

2.4. Preparation of 0.5 wt% Pt loaded CeO$_2$ by ethylene glycol reduction (EGR) method

Typically, 500 mg of either CeO$_2$−NH or CeO$_2$−CH sample was thoroughly dispersed in a 3:1 solution of ethylene glycol/water by ultrasonication for 1 h followed by constant stirring for 12 h. Afterwards, appropriate amount of H$_2$PtCl$_6$·6H$_2$O dissolved in ethylene glycol solution was drop-wise added to the above mixture and the resulting solution mixture was further stirred for 12 h. The constantly stirred reaction mixture was then refluxed at 140 °C for 12 h using a conventional oil bath. The reflux treatment at elevated temperature essentially facilitates the reduction of H$_2$PtCl$_6$·6H$_2$O to metallic Pt. The reaction mixture was then allowed to cool to room temperature and the Pt loaded CeO$_2$ sample was concentrated using centrifugation followed by washing with water, mixture of water and ethanol, and ethanol to remove adsorbed ethylene glycol from the sample. The sample was dried at 60 °C under vacuum for overnight and then calcined at 500 °C (with a heating ramp of 5 °C min^{-1}) for 3 h in flowing air to obtain the Pt loaded CeO$_2$ sample. The weight loading of Pt on the CeO$_2$ samples was fixed at 0.5% and the samples prepared using CeO$_2$−NH and
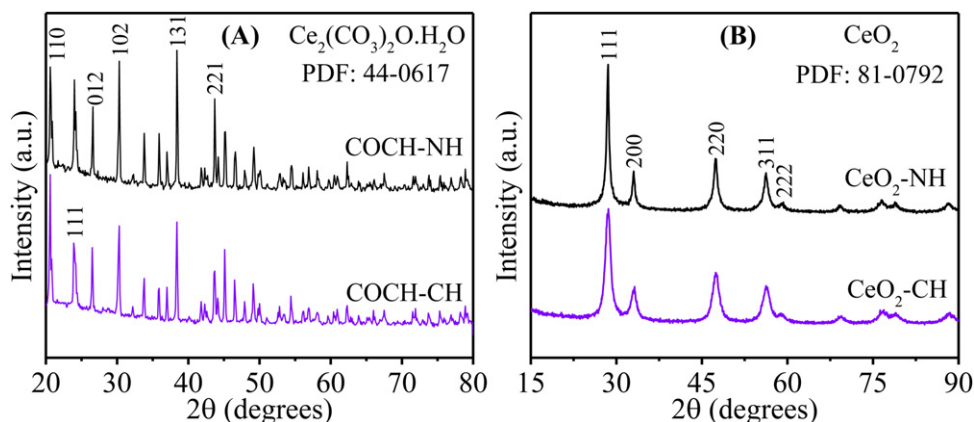
Fig. 1. PXRD patterns of (A) COCH—NH and COCH—CH precursors and (B) CeO$_2$—CH and CeO$_2$—NH samples.

CeO$_2$—CH as supports were designated as Pt/CeO$_2$—NH_EGR and Pt/CeO$_2$—CH_EGR, respectively.

2.5. Characterization

Powder X-ray diffraction (PXRD) patterns were obtained at a scan rate of 0.01°/s, using Cu K$_\alpha$ (λ = 0.15408 nm) radiation generated at 40 kV and 30 mA, in a Bruker AXS D8 Advance diffractometer. The crystallite sizes were estimated using the Scherrer equation, $D = K\lambda/(\beta \cos\theta)$ where D is the linear dimension of the crystallite, K is the spherical shape factor (taken as 0.89) and β is the full width at half maximum (FWHM) of the characteristic diffraction peaks. The multipoint N$_2$ adsorption–desorption experiments were carried out using an automatic Micromeritics ASAP 2020 analyzer. The samples were degassed at 100 °C for 2 h followed by a heat treatment at 250 °C for 10 h under a dynamic vacuum before N$_2$-physisorption measurements at liquid nitrogen temperature. The specific surface area values (SBET) were calculated using the Brunauer–Emmett–Teller (BET) equation and the porosity distributions in the samples were evaluated by the Barrett–Joyner–Halenda (BJH) method fitted to a cylindrical pore model. Field emission scanning electron microscopy (FESEM) analyses were carried out in a FEI Quanta 200 instrument. The powder samples were dispersed on a conducting carbon tape for FESEM analysis. High resolution transmission electron microscopy (HRTEM) images were collected in a Philips CM 200 transmission electron microscope with a LaB6 filament and equipped with an ultratwin objective lens. Images were acquired by using a CCD camera. The energy dispersive X-ray spectroscopy (EDS) analyses were performed using an EDAX detector attached to the TEM. The samples were thoroughly dispersed in 2-propanol by ultrasonication and drop casted on a carbon coated copper grid for HRTEM analysis. The FT-Raman spectra were measured in a LabRAM-HR Raman spectrophotometer operating at 632.81 nm excitation line of He–Ne laser in 180° back scattering geometry and with a spectral resolution of 0.3–1.0 cm^{-1}.

Temperature programmed reduction (TPR) experiments were carried out in a Micromeritics Chemisorb 2750 TPD/TPR system equipped with a thermal conductivity detector (TCD). Before a typical H$_2$-TPR experiment, ~80 mg of the sample loaded in a U-shaped quartz tube was treated with flowing O$_2$ (20%)/He (25 mL min^{-1}) at 250 °C for 1 h followed by cooling to room temperature under flowing He. The TPR patterns were recorded by slowly heating the pretreated sample at 10 °C min^{-1} to 950 °C under constant H$_2$ (5%)/He flow (20 mL min^{-1}). For estimating the oxygen storage capacity (OSC), the CeO$_2$ samples were reduced at 500 °C with H$_2$ (5%)/He flow (20 mL min^{-1}) and cooled to 400 °C in He flow. Subsequently, calibrated amount of oxygen pulses were injected periodically into the reactor until zero consumption of oxygen by

the CeO$_2$ samples occurred. The OSC values reported here show the total oxygen consumed by the individual CeO$_2$ samples during the O$_2$-pulse chemisorptions measurements.

H$_2$-chemisorption experiments were carried out in a Micromeritics ASAP 2020C instrument. The samples were subjected to cleaning in O$_2$ (5%)/Ar flow at 300 °C for 30 min and then reduction by H$_2$ (5%)/Ar flow at 150 °C for 1 h before chemisorptions measurements. The samples were degassed at 300 °C for 4 h and the chemisorption measurements were performed using H$_2$ in the low pressure range (2–20 Torr) at −90 °C. The amount of irreversible chemisorbed hydrogen was estimated by fitting the linear part of the isotherm. The inductively coupled plasma optical emission spectrometry (ICP-OES) analyses were performed in a PerkinElmer Optima 5300 DV optical emission spectrometer.
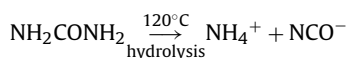
2.6. CO oxidation measurements

CO oxidation activities of the samples were conducted at atmospheric pressure. In a typical reaction, ~40 mg of the as prepared Pt/CeO$_2$ sample was placed in a U-shaped, quartz microreactor with internal diameter of 4 mm and subjected to dual pretreatment, the first at 350 °C (temperature ramp of 10 °C min^{-1} from room temperature) in a flowing mixture of 5% O$_2$/95% Ar, at 40 mL min^{-1} for 30 min. The second pretreatment was performed by cooling the sample to 150 °C after first pretreatment, and then exposing to 47.5% H$_2$ in Ar for 1 h. The pretreated sample was then allowed to cool to room temperature and the CO oxidation reaction was performed under a total gas flow rate of 48.0 mL min^{-1} to maintain a gas hourly space velocity (GHSV) of ~75,000 mL g^{-1} h^{-1}. The feed gas used for the reaction was 1.0 vol.% CO and 4.0 vol.% O$_2$ in Ar, and the temperature ramp was set at 2 °C min^{-1}. A mass spectrometer (Hyden Analytical HPR20) operating at an acquisition time of the order of 1 point every 12 s was used to analyze reactants and products. The conversion of CO was calculated from the decrease in the characteristic m/z 28 signal corrected for the CO$_2$ cracking pattern.

3. Results and discussions

3.1. PXRD, FESEM and BET analyses of CeO$_2$ samples

The PXRD patterns of COCH—NH and COCH—CH samples in Fig. 1A show characteristics peaks of orthorhombic Ce$_2$(CO$_3$)$_2$·H$_2$O phase (JCPDS: 44-0617). The following reactions occur during the nucleation of Ce$_2$(CO$_3$)$_2$·H$_2$O under homogeneous precipitation condition [26]:
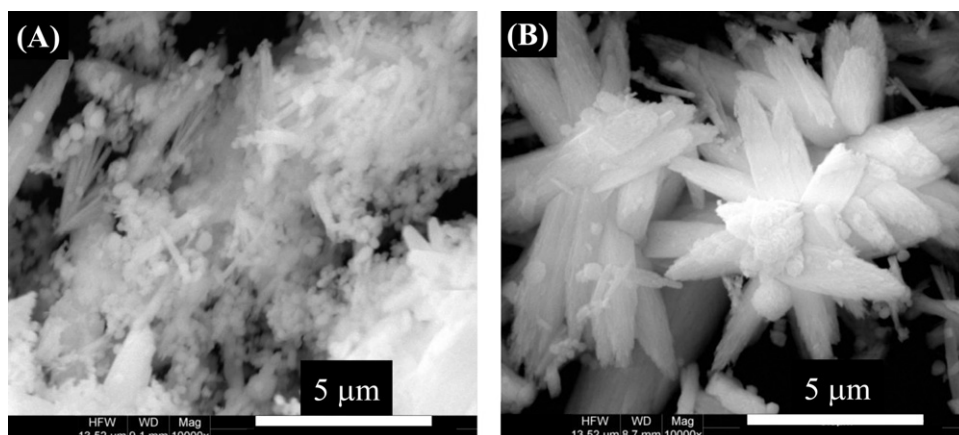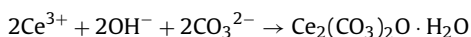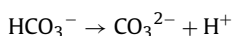
$$NH_2CONH_2 \xrightarrow[\text{hydrolysis}]{120°C} NH_4^+ + NCO^-$$

Fig. 2. FESEM images of (A) COCH—CH and (B) COCH—NH samples.

$$NCO^- + 3H_2O \rightarrow HCO_3^- + NH_4^+ + OH^-$$

$$HCO_3^- \rightarrow CO_3^{2-} + H^+$$

$$2Ce^{3+} + 2OH^- + 2CO_3^{2-} \rightarrow Ce_2(CO_3)_2O \cdot H_2O$$

From the PXRD patterns, it can be observed that the corresponding diffraction peak intensities of COCH—NH sample are higher than the COCH—CH sample. This essentially suggests that the NO_3^- ion induces higher crystallinity in the product as compared to the Cl^- ion. Further, it can be observed that the intensity of (1 1 0) peak in the COCH—CH sample is much higher than that of COCH—NH sample, which clearly indicates that the Cl^- ions induce the crystal growth of orthorhombic $Ce_2(CO_3)_2O \cdot H_2O$ along the (1 1 0) direction. The phase characteristics of the thermally decomposed products (CeO_2—CH and CeO_2—NH) were analyzed from their corresponding PXRD patterns in Fig. 1B which demonstrate prominent peaks at 28.6°, 33.1°, 47.5°, 56.3° and 59.1° corresponding to the (1 1 1), (2 0 0), (2 2 0), (3 1 1) and (2 2 2) planes, respectively, of FCC type CeO_2. The absence of additional peaks in the PXRD patterns of CeO_2 samples suggests the total decomposition of $Ce_2(CO_3)_2O \cdot H_2O$ to CeO_2. The crystallite sizes were estimated from the characteristic diffractions of (1 1 1), (2 2 0) and (3 1 1) family of planes using Scherrer equation and the average crystallite sizes of the CeO_2—CH and CeO_2—NH samples are calculated to be 7.5 and 16.4 nm, respectively.

The influence of different anions on the structural identities of the samples was investigated from the FESEM analysis of the $Ce_2(CO_3)_2O \cdot H_2O$ precursors and the corresponding CeO_2 samples, and the results are shown in Figs. 2 and 3. From the FESEM images, it is evident that, the COCH—CH sample possesses a mixture of nanosphere and microrod type surface morphology, whereas the COCH—NH sample shows a uniform microflower like surface morphology. From a closer look at the microscopic image of the COCH—CH sample, it can be seen that the microrods are essentially structured from the directional arrangement of nanospheres. Literature shows that the presence of different supplementary species, like ions and surfactants modulate the relative surface energy and the structural as well as organizational anisotropy of the growing crystals due to the occurrence of various interactions like hydrogen bonding, van der Waals forces, hydrophobic interactions and electrostatic as well as dipolar fields in the reaction medium, which essentially direct the formation of specific faceted structures [30]. In this context, the greater roles of anions like Cl^- and NO_3^- in modulating the surface morphologies of CeO_2 are well known in the literature [26,31]. In the present study, the difference in surface morphologies of the $Ce_2(CO_3)_2O \cdot H_2O$ precursors can also be attributed to the characteristic coordinating efficiency of Cl^- and NO_3^- ions, since the other chemical and thermodynamic parameters are essentially the same in the reaction medium.

From the surface morphological characteristics of the $Ce_2(CO_3)_2O \cdot H_2O$ precursors, it is assumed that the energetically favorable nanospheres are primarily nucleated from the nascent nanocrystals in the reaction medium, which then undergo
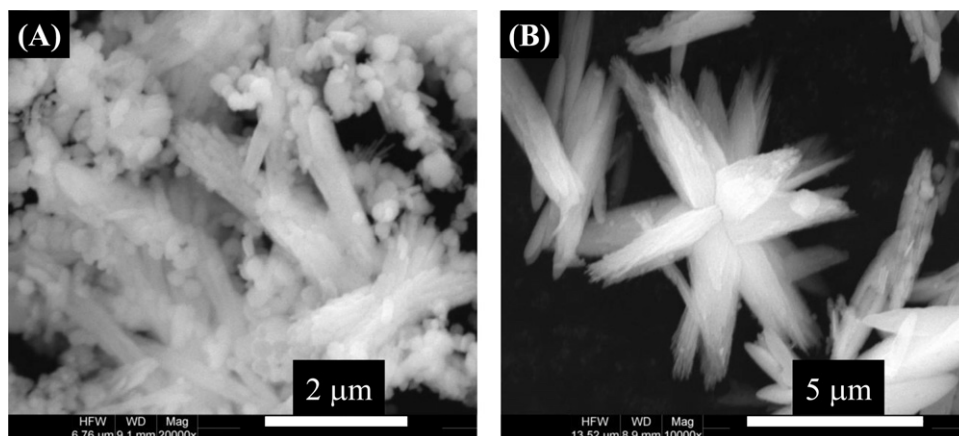

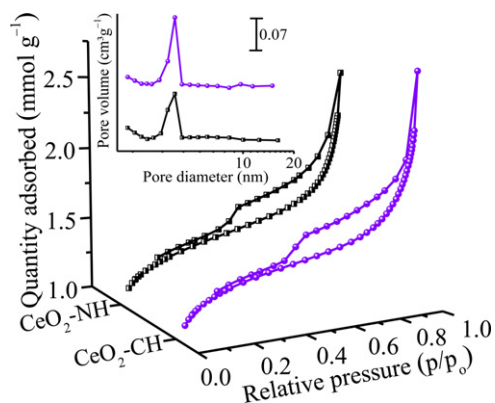**Fig. 3.** FESEM images of (A) CeO_2—CH and (B) CeO_2—NH samples.

Fig. 4. BET isotherms of the CeO₂—CH and CeO₂—NH samples; inset shows the corresponding pore size distribution profiles of the samples.

Fig. 5. Raman spectra of CeO₂—CH and CeO₂—NH samples.

multiple coalescence and Ostwald ripening to produce larger spheres [32]. Gradually, the spheres go through multiple self assemblies, Ostwald ripening and oriented attachment, which results in the characteristic surface morphology of the product [32]. From the final surface morphology of the precursors, it can be hypothesized that the selective adsorption and ligating efficiency of Cl^- and NO_3^- ions play major role during the self assembly and oriented attachment process. It is known that, NO_3^- is a stronger donor ligand than Cl^- ion toward tetravalent metal ions of lanthanides [33]. In this context, the NO_3^- ions act as coordinating ligand and assist the self assembly and oriented attachment during the growth of primary microstructures. On the other hand, the Cl^- ions do not assist the self assembly and oriented attachment, and thus the final surface morphology of the corresponding precursor (COCH—CH) remains as a combination of microspheres and microrods. The hydrothermal condition and structure directing activity of CTAB which restricts random agglomeration of the ripening crystallites also play major roles during growth of microstructures. It seems that the occurrence of elevated pressure during the hydrothermal condition enhance the kinetic ripening of nascent nanospheres before they undergo self assembly and oriented attachment. This has been proposed from our recent report where, the NO_3^- and Cl^- ions under non-hydrothermal condition direct the growth of microflower and nanorod type surface morphologies, respectively, due to kinetically controlled growth of nascent crystallites before they undergo ripening, self assembly and oriented attachment. The FESEM images of the calcined products, CeO₂—NH and CeO₂—CH, in Fig. 3 show absolute retention of surface morphologies after thermal treatment at elevated temperature. This pseudomorphic transformation [34] of $Ce_2(CO_3)_2O\cdot H_2O$ to CeO_2 with clear replication of the surface morphology is significant in the context of synthesizing allied microstructures of CeO_2 from their corresponding precursors.

The BET isotherms of the CeO₂ samples are shown in Fig. 4 with the inset showing corresponding BJH pore size distribution profiles. In spite of their different morphology, it is interesting to note that both the samples show very similar profiles with typical type-IV isotherms substantiating their inherent mesoporosity and the characteristic hysteresis loops are of H3-type, which clearly reveals that the pores in the samples are due to aggregation of plate like particles [35]. The BJH pore size distribution plots show narrow monomodal profiles in the mesopore region with the maximum at ~4 nm. The estimated specific BET surface areas of the CeO₂—CH and CeO₂—NH samples are found to be ~92 and 89 $m^2\,g^{-1}$, with corresponding BJH pore volumes of ~0.092 and 0.088 $cm^3\,g^{-1}$.
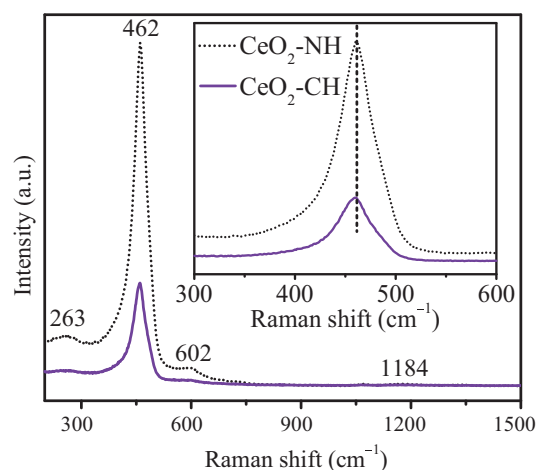
3.2. Raman analysis of CeO₂ samples

The information on the crystallinity of CeO₂ samples was obtained using Raman analysis and the characteristic Raman responses of the samples are presented in Fig. 5. The visible Raman spectral profiles of the samples essentially show typical four-band patterns with three low intense bands at ~263, 602 and 1184 cm^{-1}, attributed to second-order transverse acoustic (2TA) mode, defect-induced (D) mode due to oxygen vacancy, and second-order longitudinal optical (2LO) mode, respectively, and one high intense band at 462 cm^{-1} corresponding to the F_{2g} mode, due to the stretching of Ce—O symmetrical vibrational unit of fluorite CeO_2 [36]. However, significant difference in the intensity of the vibrational bands at 462 cm^{-1} brings up clear crystallographic distinctiveness among the CeO₂ samples. It is known that, due to reduction of the phonon lifetime in the nanocrystalline regime, an essential enhancement in intensity and asymmetry of the vibrational band occur with decrease in crystallite size [37]. From the inset of Fig. 5, it is evident that the characteristic Raman response of CeO₂—CH sample at 462 cm^{-1} is significantly lower in intensity with marginally higher asymmetry as compared to that of CeO₂—NH sample. Further, a marginal shift in the vibrational band maximum of CeO₂—CH to lower wave number as compared to the CeO₂—NH sample authenticates the variations in phonon relaxation, trivial change in the lattice parameters with decrease in the particle size and lowering in the symmetry of Ce—O bond in CeO₂—CH [36,37].

3.3. H₂-TPR and OSC analyses of CeO₂ samples

Suitable manipulation of surface area and the size as well as concentration of oxygen vacancies by microstructural modification is of utmost importance to induce reducibility in CeO₂ [38–40]. In this context, the reducibilities of CeO₂—CH and CeO₂—NH samples were investigated using H₂-TPR measurements and the corresponding reduction profiles are presented in Fig. 6. The reduction profiles of the CeO₂ samples are dominated by two major peaks, i.e. the lower temperature peak (peak I, below 550 °C) is attributed to the reduction of surface oxygen and the higher temperature peak (peak II, above 550 °C) is a result of reduction of bulk oxygen. Further, relative intensity of peak I to peak II in CeO₂—CH sample is higher than the CeO₂—NH sample. This essentially signifies enhanced surface reduction, which is attributed to the presence of higher number of effective oxygen sites and/or oxygen vacancy clusters on the surface of CeO₂—CH sample. The smaller crystallite size with lower Ce–O symmetry is possibly the origin of higher
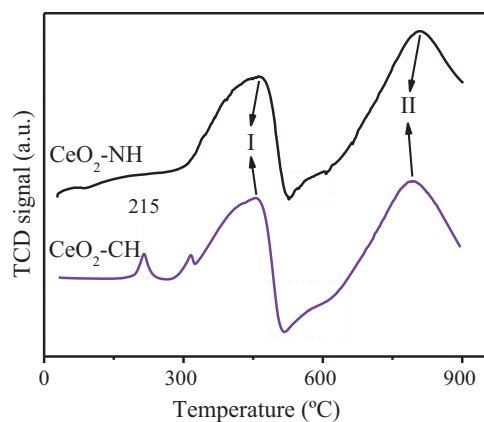
Fig. 6. H_2-TPR profiles of CeO_2—CH and CeO_2—NH samples.

Fig. 7. PXRD patterns of CeO_2—CH and CeO_2—NH samples with 0.5 wt% Pt loaded by EGR and conventional impregnation methods.

number of reactive surface oxygen sites and/or surface oxygen vacancy clusters in the CeO_2—CH sample [5,38–40]. Further, the H_2-TPR profile of CeO_2—CH sample shows unique surface reduction peaks at ~215 and 316 °C, which are absent in the CeO_2—NH sample. Recently, Zhou et al., have reported similar low temperature reduction behavior of CeO_2 nanotubes [41]. Surface area being nearly same for the CeO_2—NH and CeO_2—CH samples, the excellent low temperature surface reduction of CeO_2—CH sample suggests the presence of larger size and number of labile surface oxygen vacancy clusters. The observation of Cl^- ion inducing more surface defects in the resultant CeO_2 sample is supported by a recent report of Liu et al., which substantiates larger size oxygen vacancy cluster on CeO_2 synthesized using $CeCl_3$ as the precursor [42]. The evident negative peaks at ~520 °C in the TPR profiles of both the CeO_2 samples can be accredited to the desorption of H_2 previously incorporated into the reduced CeO_2 and/or release of CO and CH_4 from the reduction of bulk carbonate traces in the porous CeO_2 samples [43].

The quantitative OSC values of the CeO_2 samples were estimated by oxygen pulse chemisorption measurements. The CeO_2—CH sample exhibits O_2 uptake of ~455 $\mu mol\,g^{-1}$ against ~415 $\mu mol\,g^{-1}$ by CeO_2—NH sample. Theoretically, CeO_2—CH and CeO_2—NH samples with corresponding surface areas of 92 and 89 m^2g^{-1} should be able to possess 525 and 507 $\mu mol\,g^{-1}$ of O_2 with respect to an estimated 5.7 μmol of surface O_2 per m^2 of CeO_2 by assuming the involvement of two of the four oxygen sites. Accordingly, the CeO_2—CH sample sustains ~87% of the theoretical OSC against ~81% by the CeO_2—NH sample. The superior OSC of CeO_2—CH sample can be attributed to high thermal stability of surface morphology and active facets responsible for oxygen storage [6]. Further, as substantiated from the TPR results, the possibly larger size and number of oxygen vacancies on the CeO_2—CH surface also add to the superior OSC of the sample [6].

The suitable physicochemical and microstructural characteristics of CeO_2 can greatly contribute to the activity and selectivity of the noble metal loaded composite catalysts [23a,44]. In addition, the nature of noble metal dispersion is an important parameter for the catalytic performance of the composites. In this context, two different methods: (1) conventional impregnation and (2) ethylene glycol mediated reduction (EGR) of the Pt salt ($H_2PtCl_6\cdot6H_2O$) were employed to investigate the nature of Pt dispersion on the microstructurally distinctive CeO_2—CH and CeO_2—NH supports. Further, CO oxidation performances of the resulting Pt/CeO_2 composites were pursued to substantiate the effect of Pt dispersion as well as characteristic microstructure of CeO_2 on the catalytic efficiency.
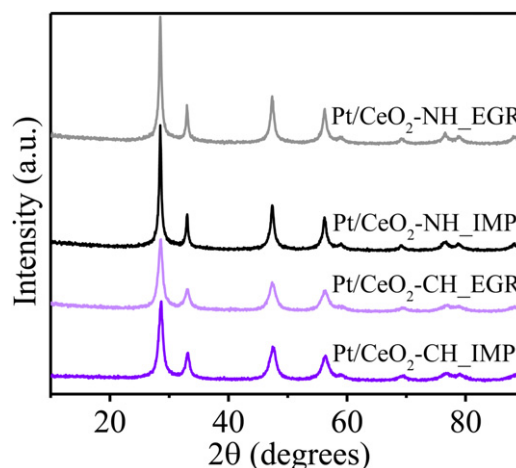
3.4. PXRD and HRTEM analyses of Pt/CeO_2 samples

The PXRD patterns of the 0.5 wt% of Pt loaded different composite samples are shown in Fig. 7. The XRD patterns are essentially dominated by the diffraction peaks due to cubic CeO_2. We also observe a total absence of diffraction peaks owing to metallic Pt. This can be attributed to the very low loading of Pt (0.5 wt%) on the Pt support. Since the PXRD analyses could not provide sufficient illumination to the nature of Pt dispersion and crystallite size, the CeO_2—CH sample with Pt loaded by EGR and impregnation methods was subjected to HRTEM analysis and the corresponding microscopic images are presented in Fig. 8. The representative HRTEM images of the Pt/CeO_2—CH_IMP sample in Fig. 8A show the presence of well faceted Pt nanoparticles with average dimension of ~3–5 nm. Further, it is evident that the Pt nanoparticles form reiterating conglomerates, with a consequent poorly extended metal–support interaction. On the contrary, no Pt particles could be distinguished from the HRTEM images of the Pt/CeO_2—CH_EGR sample in Fig. 8B. Anyway, the SAD rings clearly show the presence of Pt. This unique observation is in agreement with an extraordinarily high dispersion and very small sizes of Pt crystallites on the surface of CeO_2—CH during EG mediated reduction of $H_2PtCl_6\cdot6H_2O$. Unlike in the impregnation method, the kinetically slower rate of crystal growth during reduction of $H_2PtCl_6\cdot6H_2O$ to Pt by EG ($PtCl_6{}^{2-} + 4e^- \rightarrow Pt + 6Cl^-$) results in smaller crystallite size and very high dispersion of Pt on CeO_2 support [45]. Indeed, the ICP-OES analysis further confirmed that the Pt loadings are ~99.97–99.98% of the purposely loaded Pt on various CeO_2 samples.

3.5. H_2-chemisorption study of Pt/CeO_2 samples

The control of EGR as well as conventional impregnation methods, and microstructural affect of CeO_2 on the nature of Pt dispersion were studied by H_2-chemisorption measurements at −90 °C, this temperature being sufficiently low to arrest spill-over of hydrogen atoms onto the oxide support [46], and the results are shown in Table 1. The Pt dispersion was estimated assuming a stoichiometry of H/Pt = 1 [47]. The comparative chemisorption data shows that the CeO_2 supported composite samples prepared by EGR method provide much higher dispersion of Pt than the samples prepared by impregnation method. Further, irrespective of the adopted methods for Pt dispersion, the CeO_2—CH based composite sample shows superior H_2-adsorption as compared to the CeO_2—NH based composite sample. For instance, in both Pt/CeO_2_IMP and Pt/CeO_2_EGR samples, H adsorption per Pt site
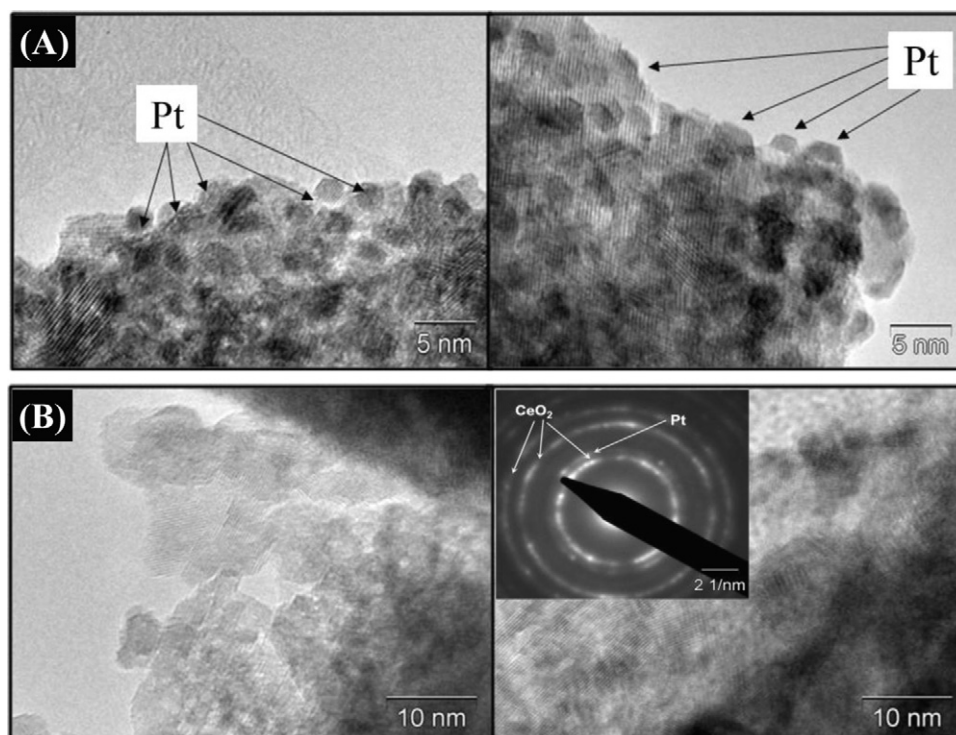
Fig. 8. HRTEM images of (A) Pt/CeO$_2$—CH_IMP and (B) Pt/CeO$_2$—CH_EGR samples. The inset in B shows the SAD information of CeO$_2$ and Pt in the corresponding sample.

(H/Pt) over the CeO$_2$—CH based samples is ≥2 times than the CeO$_2$—NH based samples. Correspondingly, the estimated exposed surface area of Pt in the CeO$_2$—CH based sample is also ≥2 times than the CeO$_2$—NH based samples. Also taking the estimated particle size from the H$_2$-chemisorption data, the overall result suggests the formation of Pt crystallites of smaller size and with high dispersion on CeO$_2$—CH based sample. Literature suggests that the presence of chlorine in the ceria support has strong negative influence on the H$_2$-chemisorptive properties [48]. In this context, the presence of elevated concentration of chloride ions in the Pt/CeO$_2$—CH composites as compared to Pt/CeO$_2$—NH composites cannot be ruled out given the type of precursor used. Nevertheless, the better H$_2$-chemisorptive properties of Pt/CeO$_2$—CH composites strongly justify the prevalence of microstructural suitability for improved surface properties of CeO$_2$ and the dispersion of metal particles [46]. As a remarkable fact, the very high dispersion of Pt crystallites after elevated temperature thermal treatment (500 °C) demonstrates the significant thermal stability of the Pt crystallites over CeO$_2$ support which may be due to the microstructural suitability of the CeO$_2$ support which prevents the sintering of highly dispersed supported Pt crystallites. This is extremely crucial in the context of utilizing the catalysts for practical application under real reaction conditions.

The rationale behind the better dispersion and smaller crystallite size of Pt on microstructurally suitable CeO$_2$ surface can be understood from the charge on different CeO$_2$ surface in the medium at which the reduction of H$_2$PtCl$_6$ has been carried out.

Table 1
H$_2$-chemisorption on various Pt/CeO$_2$ samples at −90 °C.

Sample	H/Pt	Pt surface area (m^2 g^{-1})	Particle size (nm)
Pt/CeO$_2$—CH_IMP	0.052	0.064	21.8
Pt/CeO$_2$—NH_IMP	0.026	0.032	43.8
Pt/CeO$_2$—CH_EGR	0.344	0.425	3.3
Pt/CeO$_2$—NH_EGR	0.135	0.167	8.4

It is to be noted that, CeO$_2$ acquires surface negative charge in the ethylene glycol medium which provides electrostatic suitability for interaction with growing Pt crystallites through surface O-bridge sites [49–52]. Further, unlike in CeO$_2$—NH, the CeO$_2$—CH sample possessing better nanodimensional structure expose higher concentration of active surface sites for superior dispersion of Pt nanocrystallites. Since the surface defect sites on CeO$_2$ are known to promote heterogeneous nucleation of metallic Pt nanoparticles [45], the higher number of larger size oxygen vacancy clusters on the CeO$_2$—CH sample, as identified from the TPR analysis, assist ideal crystal growth and dispersion of metallic Pt on its surface. However, during impregnation method, the thermally induced uncontrolled crystal growth results in agglomerated Pt crystallites with higher crystallite size and poor dispersion.

3.6. H$_2$-TPR study of Pt/CeO$_2$ samples

The noble metal particles are known to spill hydrogen to the redox supports even at room temperature, thereby enhancing the reducibility of the support, which is very important for oxidation reactions of molecules such as CO at sub-ambient temperatures [49,52]. In this perspective, the control of characteristic Pt dispersion and microstructure of CeO$_2$ on the reducibility of the composite samples was studied by H$_2$-TPR and the reduction profiles of Pt loaded CeO$_2$ samples by EGR as well as impregnation methods are shown in Figs. 9A and B, respectively. The TPR profiles of Pt loaded CeO$_2$ samples are clearly dominated by two major peaks; one at below 400 °C and the other one at above 400 °C, which are essentially attributed to surface and bulk reduction of CeO$_2$, respectively. It is known that, as a result of strong metal–support interaction, the CeO$_2$ supported metallic species like Pt, Ru, Ir, Au etc., in their nanosize dimensions promote the reduction of surface oxygen on CeO$_2$ due to significant molecular H$_2$ spillover from metal to the support. As a result the reduction temperature of surface CeO$_2$ decreases drastically to lower values depending on the loading of metal and surface microstructure of the support [49,52].
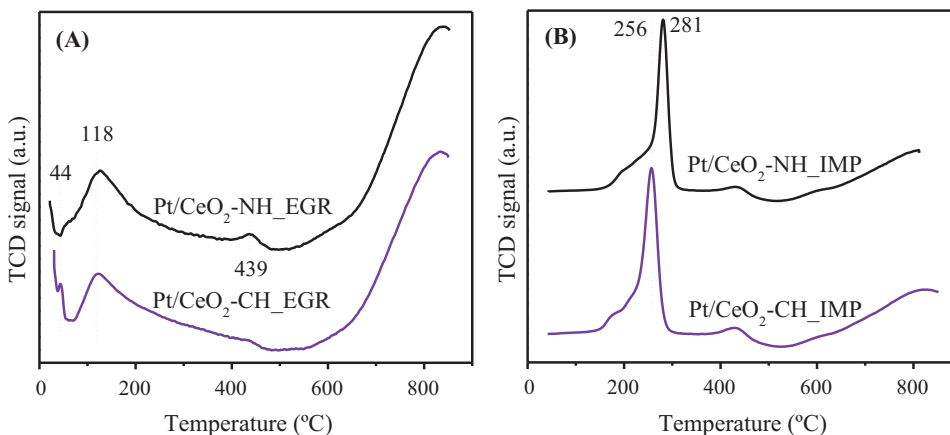
Fig. 9. H_2-TPR profiles of 0.5 wt% Pt loaded on CeO_2—CH and CeO_2—NH samples by (A) EGR and (B) IMP methods.
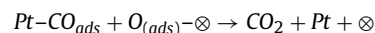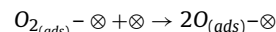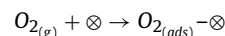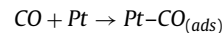
However, unless the metal loading is critically high, the characteristic reduction of bulk CeO_2 essentially remains same. Since the amount of Pt loading in our sample is very low (0.5 wt%), the typical reduction of bulk CeO_2 in all the composites remains rather similar, which can be clear if we compare the respective TPR patterns of bare CeO_2 support and Pt-loaded CeO_2 composites in Figs. 6 and 9, respectively. However, Pt loaded on CeO_2—CH samples by both EGR and impregnation methods undergo surface reduction at lower temperature as compared to the Pt loaded CeO_2—NH samples. This is essentially due to the better microstructural and surface properties of CeO_2—CH sample which possess larger size and number of labile surface oxygen vacancy clusters for facile interaction with spilling hydrogen from Pt crystallites.

The 0.5 wt% Pt dispersed CeO_2 samples prepared by impregnation methods show reduction characteristics in the similar temperature range as reported by Linganiso et al., with the surface reduction of CeO_2 at ~200–285 °C and bulk reduction at ~800 °C [53]. However, the Pt/CeO_2—CH_IMP sample undergoes surface reduction at lower temperature (peak maxima at ~256 °C) as compared to the Pt/CeO_2—NH_IMP sample (peak maxima at ~281 °C). This clearly shows the microstructural ascendancy of the CeO_2—CH sample which promotes size reduction and better dispersion of Pt crystallites [54]. The CeO_2—CH support provides more active surface area to the Pt crystallites which in effect assist spilling of more H_2 to the support for reduction at lower temperature. In comparison, the 0.5 wt% Pt dispersed CeO_2 samples prepared by EGR method show drastic decrease in the surface reduction temperature (~160 °C) as compared to the Pt dispersed on CeO_2 by impregnation method. This is essentially due to the extremely high dispersion and very small size of Pt crystallites on CeO_2 supports. This obviously indicate the exposure of higher concentrations of active Pt surface sites for superior adsorption and spilling of H_2 to the CeO_2 support for reduction at very low temperature. In addition, due to more defect sites on the CeO_2—CH sample, the strong electron transfer from Pt to Ce (due to higher degree of contact between Pt and CeO_2) makes the Ce–O bond much weak in the Pt/CeO_2—CH composite, as compared to that in the Pt/CeO_2—NH composite [3,20,55]. This results in the facile reduction of highly labile oxygen on the Pt/CeO_2—CH as compared to the poorly labile surface oxygen on Pt/CeO_2—NH composites. Small humps at ~439 °C in the TPR profiles of all the Pt loaded samples are assigned to the residual surface reduction of CeO_2 due to smaller amount of Pt (only 0.5 wt%) in the composites, which may not be sufficient to promote the reduction of complete surface of high surface area CeO_2. However, to our surprise, the hump in the Pt/CeO_2—CH_EGR sample is dramatically less intense than the other samples, in particular the Pt/CeO_2—NH_EGR sample, which substantiates that the majority of

surface reduction of CeO_2—CH is promoted by highly dispersed Pt. This clearly suggests that the Pt crystallites are effectively smaller and more dispersed in the Pt/CeO_2—CH_EGR sample as compared to the Pt/CeO_2—NH_EGR sample composite, which further confirms the prevalence of microstructural suitability of CeO_2 for the controlled growth and thus high dispersion of Pt crystallites on its surface. The broadness in the reduction peaks of Pt/CeO_2_EGR samples as compared to the Pt/CeO_2_IMP samples is due to the very small crystallite size and finely dispersed Pt over CeO_2.

3.7. CO oxidation activity of Pt/CeO_2 samples

The efficiency of CO oxidation is highly dependent on the microstructural suitability and geometry of the support as well as the supported Pt crystallites which essentially control the chemical potential of the reactants under different reaction conditions [3]. It has been proposed that during the reaction process, CO adsorbed to metal site as M–CO type configuration and O_2 activated on ceria sites react to form CO_2 via a dual site mechanism, which is depicted as follows [2–5]:

$$CO + Pt \rightarrow Pt–CO_{(ads)}$$
$$O_{2(g)} + \otimes \rightarrow O_{2(ads)} – \otimes$$
$$O_{2(ads)} – \otimes + \otimes \rightarrow 2O_{(ads)} – \otimes$$
$$Pt–CO_{ads} + O_{(ads)} – \otimes \rightarrow CO_2 + Pt + \otimes$$

where $\otimes$ symbolizes an individual site over ceria surface. Although the as illustrated mechanism does not essentially reflect the complexity of what exactly occurs at the catalytic surface during oxidation of CO, it provides a broad spectrum of possibility that the diversification in surface energies due to different microstructural characteristics of the CeO_2 support and geometrical characteristics of the supported Pt crystallites may greatly control the kinetics as well as thermodynamics of CO and O_2 adsorption and their reaction to form CO_2 [2–5,23a,56]. The geometrically different Pt crystallites supported on CeO_2 samples with different microstructure were tested for their efficiency toward CO oxidation, and the CO conversion plots against temperature are presented in Fig. 10. Interestingly, under our experimental conditions the impregnated Pt/CeO_2 samples show 100% CO oxidation in the temperature range of ~150–300 °C, whereas the Pt/CeO_2_EGR samples demonstrate 100% CO oxidation below 100 °C. Further, the Pt/CeO_2_EGR samples exhibit ~10–15% of CO oxidation even at room temperature (~30 °C). The temperature of 50% CO conversion ($T_{1/2}$) on CeO_2—CH based composites (56 °C and 211 °C for Pt/CeO_2_CH_EGR and Pt/CeO_2—CH_IMP samples, respectively) is lower than the
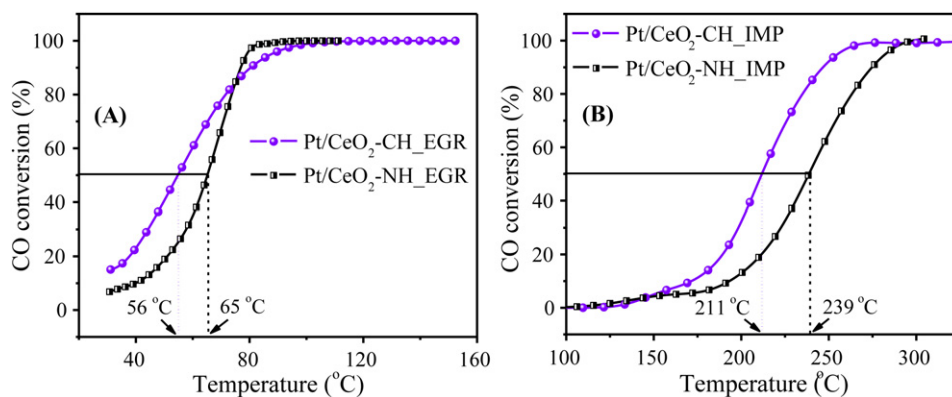
Fig. 10. Conversion of CO in the presence of O_2 over 0.5 wt% Pt loaded on CeO_2—CH and CeO_2—NH samples by (A) EGR and (B) IMP methods.

CeO_2—NH based composites (65 °C and 239 °C for Pt/CeO_2—NH_EGR and Pt/CeO_2—NH_IMP samples, respectively). Among two broad classes of active sites on a metal-oxide system, the interfacial site between metal and oxide is endowed with lower activation energy (23 kJ mol^{-1}) as compared to the site located on the bare support (44 kJ mol^{-1}) [57]. In this context, the Pt/CeO_2 interfacial sites and the CeO_2 sites at very close vicinity to Pt are essentially more active for CO oxidation reaction, although morphology of the metal nanoparticles can also greatly affect the catalytic activity [2–5,58]. Since the crystal growth of Pt (in EGR or IMP methods) over both the CeO_2 samples (CeO_2—NH and CeO_2—CH) were achieved under very similar experimental conditions, the corresponding morphology of Pt crystallites is expected to be similar in the Pt/CeO_2—CH_EGR and Pt/CeO_2—NH_EGR, or in the Pt/CeO_2—CH_IMP and Pt/CeO_2—NH_IMP samples. Hence the morphology of Pt crystallites may not be the reason behind the difference in the activity of CeO_2—CH and CeO_2—NH based composite catalysts. Therefore, the high activity of CeO_2—CH based sample is essentially due to the presence of higher concentrations of active interfacial sites (with Pt) for CO activation and oxidation. Further, the higher amount/density and larger size of oxygen vacancy clusters on CeO_2 facilitates facile adsorption of O_2 and easy diffusion of oxygen from the bulk to the surface, which is very crucial for low temperature oxidation of CO. From the Raman, TPR and OSC measurements, it is clear that the CeO_2—CH sample obviously possess larger size and number of labile surface oxygen vacancy clusters. Hence, we observe improved CO oxidation on the Pt/CeO_2—CH samples as compared to the Pt/CeO_2—NH samples. Besides, the temperatures for oxidation of CO over the Pt/CeO_2-EGR samples are exceptionally low, considering that the loading of Pt is very low. This can be ascribed to the outstanding dispersion and sub-nanometer size Pt crystallites over CeO_2 supports, when the Pt/CeO_2 nanocomposite is prepared via EGR method. Very small size of Pt crystallites possess higher numbers of defects due to numerous steps and edges, which are energetically active to facilitate adsorption of higher number of CO molecules for oxidation [59]. Further, the sub-nanometer size crystallites of Pt offer higher interfacial area to the CeO_2 support [60]. Since the highly dispersed smaller sized crystals possess numerous active Pt site clusters, according to the Blyholder model [20], the M → C π back donation becomes more significant and as a result considerable weakening of the CO bond occurs. This effectively promotes the facile oxidation of CO with lower activation energy needed. This is corroborated by the room temperature oxidation of CO over the Pt/CeO_2-EGR samples.

The presence of different oxidation states of Pt may have some effect on the CO oxidation behavior. Since in the present study, the metal loading in the samples is very low (~0.5 wt%), the precise identification of oxidation states of Pt through spectroscopic means is always troublesome and prone to error. The well established X-ray photoelectron spectroscopy (XPS) method is also found to be not so precise when analyzing very small Pt crystallites (large peak shifts due to final-state effects) on a non-conducting CeO_2 support (charging effects). Furthermore, the contrast between Pt and CeO_2 happens to be poor during XPS analysis due to large difference in the atomic number between Ce and Pt [61].

From the oxidation results, it is observed that the difference in light-off temperatures for oxidation of CO over Pt loaded CeO_2 samples prepared using impregnation and EGR methods is enormous. In addition, the trend in the efficiency of CO oxidation on the microstructurally different CeO_2 supports with same amount of Pt is similar. Hence, it can be authenticated that the difference in catalytic CO oxidation behavior on the Pt loaded CeO_2 samples prepared using impregnation and EGR methods is due to difference in size, dispersion and degree of aggregation of metallic Pt crystallites over CeO_2 supports and not due to differences in the oxidation states of Pt. Our assumption is supported by a recent report by Hinokuma et al. [19], where it has been proposed that the steady-state catalytic CO oxidation at low temperatures always requires metallic Pt species on the surface of CeO_2. Further, the similar trend in the CO oxidation efficiency on microstructurally different CeO_2 substantiates the dominating affect of microstructure in providing different degrees of active sites as well as oxygen vacancy for the characteristic catalytic behavior.

It is known that the presence of chlorine ion have a negative effect on the CO oxidation efficiency of Pt/CeO_2 [62]. However, in the present study, we find that the CeO_2 sample prepared from chloride source of cerium shows improved catalytic performance as compared to the CeO_2 sample prepared from nitrate source. In this context, the results presented here are quite interesting which cannot be explained on the basis of chloride ion effect. Further, studies show that the residual chlorine from the Pt precursors does not bring much affect in the catalytic (CO oxidation) performance of Pt/CeO_2 based composites [62]. In the present study, the loadings of Pt on the CeO_2 supports are very small (only 0.5 wt%). On the other hand, we see a significant decrease (~150–170°) in the light-off temperature for CO oxidation on the Pt/CeO_2 samples prepared via EGR method as compared to the samples prepared via IMP method. So, we do not expect such a huge change in the CO oxidation efficiency due to the presence of only trivial amount of more chloride ion in the Pt/CeO_2 samples prepared via IMP method. Hence it is obvious that the improved CO oxidation efficiencies of Pt/CeO_2 samples prepared via EGR method are mostly due to the smaller size and exceptionally finer dispersion of Pt crystallites.

4. Conclusions

In the present study, we have demonstrated the anion (Cl$^-$ and NO$_3^-$) induced selective micro-structurization of CeO$_2$ under hydrothermal mediated homogeneous precipitation conditions. The H$_2$-TPR and oxygen pulse chemisorptions measurements reveal low temperature reducibility and higher OSC of the CeO$_2$ sample synthesized via Cl$^-$ as the counter anion. These results along with the Raman spectral studies demonstrate that Cl$^-$ induces higher lattice defects and oxygen vacancy in the resultant CeO$_2$ sample. Further, 0.5 wt% of Pt was supported on the CeO$_2$ samples via impregnation and ethylene glycol mediated reduction of H$_2$PtCl$_6$·6H$_2$O. The TEM analyses show that unlike in impregnated samples where the Pt particles are heavily agglomerated, the Pt crystallites are highly dispersed on the CeO$_2$ support when prepared via ethylene glycol mediated reduction method. This is due to kinetically slower growth of Pt crystallites during the reduction of H$_2$PtCl$_6$·6H$_2$O by ethylene glycol. Further, in H$_2$-TPR study, the Pt/CeO$_2$ sample prepared by ethylene glycol mediated reduction method show low temperature surface reducibility as compared to the Pt/CeO$_2$ sample prepared by impregnation method. The H$_2$-TPR study also shows better Pt dispersion and promoting activity of CeO$_2$ sample synthesized in the presence of Cl$^-$ ion. The H$_2$-chemisorption results further validate the smaller size and better dispersion of Pt crystallites when synthesized by ethylene glycol mediated reduction method. The CO oxidation studies in the presence of O$_2$ demonstrate exceptionally lower temperature CO oxidation activity (100% conversion in <100 °C) of Pt/CeO$_2$ hetero-nanocomposites prepared by ethylene glycol mediated reduction method as compared to the sample prepared by impregnation method (100% conversion at ~300 °C). Further, irrespective of the method used for Pt dispersion, the Pt/CeO$_2$ hetero-nanocomposites based on the CeO$_2$ synthesized in the presence of Cl$^-$ ions show lower temperature CO oxidation as compared to the nanocomposites based on the CeO$_2$ synthesized in the presence of NO$_3^-$ ions. The exceptionally finer dispersion of Pt crystallites during ethylene glycol mediated reduction of H$_2$PtCl$_6$·6H$_2$O, and higher number of oxygen vacancies as well as active surface sites of CeO$_2$ synthesized in the presence of Cl$^-$ ions altogether provide large number of active Pt/CeO$_2$ interfaces for facile oxidation of CO at very low temperature. Although the mechanistic aspects of the enhanced CO oxidation activity on suitable Pt/CeO$_2$ hetero-nanocomposites are still to be understood fully, the overall finding reveals adequate promise in terms of developing novel metal supported nanocomposites for applications in heterogeneous catalysis.

Acknowledgments

References

[1] (a) J.E. Mondloch, E. Bayram, R.G. Finke, Journal of Molecular Catalysis A: Chemical 355 (2012) 1–38;
(b) S.L. Wegener, T.J. Marks, P.C. Stair, Accounts of Chemical Research 45 (2012) 206–214.
[2] S. Royer, D. Duprez, ChemCatChem 3 (2011) 24–65.
[3] H. Freund, G. Meijer, M. Scheffler, R. Schlögl, M. Wolf, Angewandte Chemie International Edition 50 (2011) 10064–10094.
[4] A.D. Allian, K. Takanabe, K.L. Fujdala, X. Hao, T.J. Truex, J. Cai, C. Buda, M. Neurock, E. Iglesia, Journal of the American Chemical Society 133 (2011) 4498–4517.
[5] Z. Wang, Q. Wang, Y. Liao, G. Shen, X. Gong, N. Han, H. Liu, Y. Chen, ChemPhysChem 12 (2011) 2763–2770.
[6] J. Zhang, H. Kumagai, K. Yamamura, S. Ohara, S. Takami, A. Morikawa, H. Shinjoh, K. Kaneko, T. Adschiri, A. Suda, Nano Letters 11 (2011) 361–364.
[7] C. Daniel, M.-O. Clarté, S.-P. Teh, O. Thinon, H. Provendier, A.C.V. Veen, B.J. Beccard, Y. Schuurman, C. Mirodatos, Journal of Catalysis 272 (2010) 55–64.
[8] M. Cargnello, N.L. Wieder, T. Montini, R.J. Gorte, P. Fornasiero, Journal of the American Chemical Society 132 (2010) 1402–1409.
[9] A.A. Herzing, C.J. Kiely, A.F. Carley, P. Landon, G.J. Hutchings, Science 321 (2008) 1331–1335.
[10] D.S. Afanasev, O.A. Yakovina, N.I. Kuznetsova, A.S. Lisitsyn, Catalysis Communications 22 (2012) 43–47.
[11] S.H. Joo, J.Y. Park, J.R. Renzas, D.R. Butcher, W. Huang, G.A. Somorjai, Nano Letters 10 (2010) 2709–2713.
[12] (a) G.S. Zafiris, R.J. Gorte, Journal of Catalysis 143 (1993) 86–91;
(b) D.W. Goodman, C.H.F. Peden, M.S. Chen, Surface Science 603 (2007) L124–L126;
(c) J. Gustafson, R. Westerström, O. Balmes, A. Resta, R. Rijn, X. Torrelles, C.T. Herbschleb, J.W.M. Frenken, E. Lundgren, Journal of Physical Chemistry C 114 (2010) 4580–4583.
[13] X. Bokhimi, R. Zanella, C. Angeles-Chavez, Journal of Physical Chemistry C 114 (2010) 14101–14109.
[14] T. Jin, T. Okuhara, G.J. Mains, J.M. White, Journal of Physical Chemistry 91 (1987) 3310–3315.
[15] (a) P. Bera, K.C. Patil, V. Jayaram, G.N. Subbanna, M.S. Hegde, Journal of Catalysis 196 (2000) 293–301;
(b) P. Bera, A. Gayen, M.S. Hegde, N.P. Lalla, L. Spadaro, F. Frusteri, F. Arena, Journal of Physical Chemistry B 107 (2003) 6122–6130.
[16] Q. Fu, H. Saltsburg, M. Flytzani-Stephanopoulos, Science 301 (2003) 935–938.
[17] H.-P. Zhou, H.-S. Wu, J. Shen, A.-X. Yin, L.-D. Sun, C.-H. Yan, Journal of the American Chemical Society 132 (2010) 4998–4999.
[18] P.-A. Carlsson, M. Skoglundh, Applied Catalysis B: Environmental 101 (2011) 669–675.
[19] S. Hinokuma, H. Okamoto, E. Ando, K. Ikeue, M. Machida, Bulletin of Chemical Society of Japan 85 (2012) 144–149.
[20] G. Blyholder, Journal of Physical Chemistry 68 (1964) 2772–2777.
[21] M. Hatanaka, N. Takahashi, T. Tanabe, Y. Nagai, K. Dohmae, Y. Aoki, T. Yoshida, H. Shinjoh, Applied Catalysis B: Environmental 99 (2010) 336–342.
[22] (a) A. Trovarelli, Catalysis by Ceria and Related Materials, Catalysis Science Series, Imperial College Press, London, 2002 (and references there in;);
(b) J. Kašpar, P. Fornasiero, M. Graziani, Catalysis Today 50 (1999) 285–298;
(c) D. Barreca, A. Gasparotto, E. Tondello, C. Sada, S. Polizzi, A. Benedetti, Chemical Vapor Deposition 9 (2003) 199–206;
(d) C.T. Campbell, C.H.F. Peden, Science 309 (2005) 713–714;
(e) H. Imagawa, A. Suda, K. Yamamura, S. Sun, Journal of Physical Chemistry C 115 (2011) 1740–1745.
[23] (a) D. Barreca, E. Comini, A. Gasparotto, C. Maccato, C. Maragno, G. Sberveglieri, E. Tondello, Journal of Nanoscience and Nanotechnology 8 (2008) 1012–1016;
(b) R. Si, M. Flytzani-Stephanopoulos, Angewandte Chemie International Edition 47 (2008) 2884–2887;
(c) G.R. Patzke, Y. Zhou, R. Kontic, F. Conrad, Angewandte Chemie International Edition 50 (2011) 826–859;
(d) T. Li, G. Xiang, J. Zhuang, X. Wang, Chemical Communications 47 (2011) 6060–6062;
(e) K. Zhou, Y. Li, Angewandte Chemie International Edition 51 (2012) 602–613.
[24] (a) D. Barreca, A. Gasparotto, C. Maccato, C. Maragno, E. Tondello, E. Comini, G. Sberveglieri, Nanotechnology 18 (2007) 125502 (6pp);
(b) Q. Yuan, H.-H. Duan, L.-L. Li, L.-D. Sun, Y.-W. Zhang, C.-H. Yan, Journal of Colloid and Interface Science 335 (2009) 151–167;
(c) D. Wang, Y. Kang, V. Doan-Nguyen, J. Chen, R. Küngas, N.L. Wieder, K. Bakhmutsky, R.J. Gorte, C.B. Murray, Angewandte Chemie International Edition 50 (2011) 4378–4381.
[25] K. Zhou, X. Wang, X. Sun, Q. Peng, Y. Li, Journal of Catalysis 229 (2005) 206–212.
[26] S.K. Meher, G. Ranga Rao, Journal of Colloid and Interface Science 373 (2012) 46–56.
[27] (a) K.M. Bratlie, H. Lee, K. Komvopoulos, P. Yang, G.A. Somorjai, Nano Letters 7 (2007) 3097–3101;
(b) Y. Xia, Y. Xiong, B. Lim, S.E. Skrabalak, Angewandte Chemie International Edition 48 (2009) 60–103;
(c) B. Lim, Y. Xia, Angewandte Chemie International Edition 50 (2011) 76–85.
[28] (a) T. Engel, G. Ertl, Advances in Catalysis 28 (1979) 1–78;
(b) A.K. Santra, D.W. Goodman, Electrochimica Acta 47 (2002) 3595–3609.
[29] (a) A. Bourane, S. Derrouiche, D. Bianchi, Journal of Catalysis 228 (2004) 288–297;
(b) B. Qiao, A. Wang, X. Yang, L.F. Allard, Z. Jiang, Y. Cui, J. Liu, J. Li, T. Zhang, Nature Chemistry 3 (2011) 634–641;
(c) G.N. Vayssilov, Y. Lykhach, A. Migani, T. Staudt, G.P. Petrova, N. Tsud, T. Skála,

A. Bruix, F. Illas, K.C. Prince, V. Matolín, K.M. Neyman, J. Libuda, Nature Materials 10 (2011) 310–315.

[30] (a) X.-Y. Yang, A. Léonard, A. Lemaire, G. Tian, B.-L. Su, Chemical Communications 47 (2011) 2763–2786;
(b) D.J. Mowbray, J.I. Martínez, F. Calle-Vallejo, J. Rossmeisl, K.S. Thygesen, K.W. Jacobsen, J.K. Nørskov, Journal of Physical Chemistry C 115 (2011) 2244–2252.

[31] Q. Wu, F. Zhang, P. Xiao, H. Tao, X. Wang, Z. Hu, Y. Lu, Journal of Physical Chemistry C 112 (2008) 17076–17080.

[32] (a) H. Cölfen, M. Antonietti, Angewandte Chemie International Edition 44 (2005) 5576–5591;
(b) M. Grzelczak, J. Vermant, E.M. Furst, L.M. Liz-Marzán, ACS Nano 4 (2010) 3591–3605.

[33] J.G.H. du Preez, C.P.J.V. Vuuren, Journal of Inorganic and Nuclear Chemistry 36 (1974) 81–85.

[34] (a) J.C. Lytle, N.R. Denny, R.T. Turgeon, A. Stein, Advanced Materials 19 (2007) 3682–3686;
(b) Y. Shi, F. Zhang, Y.-S. Hu, X. Sun, Y. Zhang, H.I. Lee, L. Chen, G.D. Stucky, Journal of the American Chemical Society 132 (2010) 5552–5553.

[35] F. Rouquerol, J. Rouquerol, K. Sing, Adsorption by Powders and Porous Solids, Academic Press, London, 1999.

[36] Z. Wu, M. Li, J. Howe, H.M. Meyer, S.H. Overbury, Langmuir 26 (2010) 16595–16606.

[37] (a) J.E. Spanier, R.D. Robinson, F. Zhang, S.-W. Chan, I.P. Herman, Physical Review B 64 (2001), 245407 (1-8);
(b) J. Guzman, S. Carrettin, A. Corma, Journal of the American Chemical Society 127 (2005) 3286–3287;
(c) M. Guo, J. Lu, Y. Wu, Y. Wang, M. Luo, Langmuir 27 (2011) 3872–3877.

[38] (a) P. Fornasiero, R. Di Monte, G. Ranga Rao, J. Kašpar, S. Meriani, A. Trovarelli, M. Graziani, Journal of Catalysis 151 (1995) 168–177;
(b) G. Ranga Rao, P. Fornasiero, R. Di Monte, J. Kašpar, G. Vlaic, G. Balducci, S. Meriani, G. Gubitosa, A. Cremona, M. Graziani, Journal of Catalysis 162 (1996) 1–9;
(c) F. Esch, S. Fabris, L. Zhou, T. Montini, C. Africh, P. Fornasiero, G. Comelli, R. Rosei, Science 309 (2005) 752–755.

[39] G. Ranga Rao, Bulletin of Materials Science 22 (1999) 89–94.

[40] G. Zhou, P.R. Shah, T. Montini, P. Fornasiero, R.J. Gorte, Surface Science 601 (2007) 2512–2519.

[41] K. Zhou, Z. Yang, S. Yang, Chemistry of Materials 19 (2007) 1215–1217.

[42] X. Liu, K. Zhou, L. Wang, B. Wang, Y. Li, Journal of the American Chemical Society 131 (2009) 3140–3141.

[43] F. Fajardie, J.-F. Tempere, J.-M. Manoli, G. Djega-Mariadassou, G. Blanchard, Journal of Chemical Society, Faraday Transaction 94 (1998) 3727–3735.

[44] (a) Z.-Y. Yuan, V. Idakiev, A. Vantomme, T. Tabakova, T.-Z. Ren, B.-L. Su, Catalysis Today 131 (2008) 203–210;
(b) J.B. Park, J. Graciani, J. Evans, D. Stacchiola, S. Ma, P. Liu, A. Nambu, J.F. Sanz, J. Hrbek, J.A. Rodriguez, Proceedings of the National Academy of Sciences of the United States of America 106 (2009) 4975–4980;
(c) M.B. Boucher, S. Goergen, N. Yi, M. Flytzani-Stephanopoulos, Physical Chemistry Chemical Physics 13 (2011) 2517–2527.

[45] E.A. Anumol, P. Kundu, P.A. Deshpande, G. Madras, N. Ravishankar, ACS Nano 5 (2011) 8049–8061.

[46] J.M. Gatica, R.T. Baker, P. Fornasiero, S. Bernal, J. Kašpar, Journal of Physical Chemistry B 105 (2001) 1191–1199.

[47] (a) B.J. Kip, F.B.M. Duivenvoorden, D.C. Koningsberger, R. Prins, Journal of Catalysis 105 (1987) 26–38;
(b) C. Mager-Maury, G. Bonnard, C. Chizallet, P. Sautet, P. Raybaud, ChemCatChem 3 (2011) 200–207.

[48] D.I. Kondarides, X.E. Verykios, Journal of Catalysis 174 (1998) 52–64.

[49] (a) Y. Ji, A.M.J. van der Eerden, V. Koot, P.J. Kooyman, J.D. Meeldijk, B.M. Weckhuysen, D.C. Koningsberger, Journal of Catalysis 234 (2005) 376–384;
(b) A.Y. Stakheev, Y. Zhang, A.V. Ivanov, G.N. Baeva, D.E. Ramaker, D.C. Koningsberger, Journal of Physical Chemistry C 111 (2007) 3938–3948.

[50] A. Bumajdad, M.I. Zaki, J. Eastoe, L. Pasupulety, Langmuir 20 (2004) 11223–11233.

[51] (a) Y. Nagai, T. Hirabayashi, K. Dohmae, N. Takagi, T. Minami, H. Shinjoh, S. Matsumoto, Journal of Catalysis 242 (2006) 103–109;
(b) Y. Nagai, K. Dohmae, Y. Ikeda, N. Takagi, T. Tanabe, N. Hara, G. Guilera, S. Pascarelli, M.A. Newton, O. Kuno, H. Jiang, H. Shinjoh, S. Matsumoto, Angewandte Chemie International Edition 47 (2008) 9303–9306.

[52] (a) J.T. Miller, B.L. Meyers, F.S. Modica, G.S. Lane, M. Vaarkamp, D.C. Koningsberger, Journal of Catalysis 43 (1993) 395–408;
(b) T. Takeguchi, S. Manabe, R. Kikuchi, K. Eguchi, T. Kanazawa, S. Matsumoto, W. Ueda, Applied Catalysis A: General 293 (2005) 91–96;
(c) G. Dutta, U.V. Waghmare, T. Baidya, M.S. Hegde, Chemistry of Materials 19 (2007) 6430–6436.

[53] L.Z. Linganiso, G. Jacobs, K.G. Azzam, U.M. Graham, B.H. Davis, D.C. Cronauer, A.J. Kropf, C.L. Marshall, Applied Catalysis A: General 394 (2011) 105–116.

[54] J.A. Farmer, C.T. Campbell, Science 329 (2010) 933–936.

[55] J. Guzman, S. Carrettin, J.C. Fierro-Gonzalez, Y. Hao, B.C. Gates, A. Corma, Angewandte Chemie International Edition 44 (2005) 4778–4781.

[56] (a) A. Holmgren, B. Andersson, D. Duprez, Applied Catalysis B: Environmental 22 (1999) 215–230;
(b) L.C. Grabow, B. Hvolbæk, J.K. Nørskov, Topics in Catalysis 53 (2010) 298–310.

[57] S.O. Shekhtman, A. Goguet, R. Burch, C. Hardacre, N. Maguire, Journal of Catalysis 253 (2008) 303–311.

[58] L. Xu, Y. Ma, Y. Zhang, Z. Jiang, W. Huang, Journal of the American Chemical Society 131 (2009) 16366–16367.

[59] (a) A. Martínez-Arias, J.M. Coronado, R. Catalun, J.C. Conesa, J. Soria, Journal of Physical Chemistry B 102 (1998) 4357–4365;
(b) Z. Zhou, S. Kooi, M. Flytzani-Stephanopoulos, H. Saltsburg, Advanced Functional Materials 18 (2008) 2801–2807;
(c) M. Happel, J. Mysliveček, V. Johanek, F. Dvořák, O. Stetsovych, Y. Lykhach, V. Matolin, J. Libuda, Journal of Catalysis 289 (2012) 118–126;
(d) H. Yoshida, Y. Kuwauchi, J.R. Jinschek, K. Sun, S. Tanaka, M. Kohyama, S. Shimada, M. Haruta, S. Takeda, Science 335 (2012) 317–319.

[60] C.M.Y. Yeung, K.M.K. Yu, Q.J. Fu, D. Thompsett, M.I. Petch, S.C. Tsang, Journal of the American Chemical Society 127 (2005) 18010–18011.

[61] M. Cargnello, T. Montini, S. Polizzi, N.L. Wieder, R.J. Gorte, M. Graziani, P. Fornasiero, Dalton Transactions 39 (2010) 2122–2127.

[62] U. Oran, D. Uner, Applied Catalysis B: Environmental 54 (2004) 183–191.